Closed-Loop Control of a Tendon-Driven Active Needle for Tip Tracking at Desired Bending Angle inside a Water Medium using Ultrasound or EM Tracker Feedback for High-Dose-Rate Prostate Brachytherapy

Samuel Lafreniere, Blayton Padasdao, Bardia Konh[1]

Department of Mechanical Engineering

University of Hawaii at Manoa

[1] Corresponding author. Mail: 2540 Dole St., Holmes Hall 302, Honolulu, HI 96822. Email address: konh@hawaii.edu

Abstract

Prostate cancer is the second most common malignancy in American men. High-dose-rate brachytherapy is a popular treatment technique in which a large, localized radiation dose is used to kill cancer. Utilization of curvilinear catheter implantation inside the prostate gland to provide access channels to host the radiation source is under investigation by our group. To this aim, we have introduced an active needle to curve inside the prostate conformal to the patient's specific anatomical relationship for improved dose distribution to the prostate and reduced toxicity to the organs at risk (OARs). This work presents closed-loop control of our tendon-driven active needle in water medium and air using the position feedback of the tip obtained in real time from an ultrasound (US) or an electromagnetic (EM) tracking sensor, respectively. The active needle consists of a flexure compliant section to realize bending in two directions via actuation of two internal tendons. The actuation system is developed using two Maxon motors programmed to pull the two tendons at certain displacements. An US or EM tracker sensor is used to track the tip of the robotic tool in real time and provide position feedback to the controller. Tracking errors using US and EM tracker are estimated and compared. Results show that the bending angle of the active needle could be controlled using position feedback of the US or the EM tracking system with a bending angle error of less than 1.00 degree. It is concluded that the actuation system and controller, presented in this work, are able to realize a desired bending angle at the active needle tip with reasonable accuracy.

1. Introduction

1.1. Challenges associated with needle insertion tasks

Several minimally invasive diagnostic and therapeutic procedures rely upon needle insertion techniques. The procedures' success rate depends on accurate navigation of the steerable needles and precise tip placement at target locations. Limited needle actuation and flexibility inside tissue, movement of the target during needle insertion [1], and inadequate visualization with the most practiced ultrasound (US) and magnetic resonance imaging (MRI) inside of the patient's body [2] are cited as common challenges in manual or robotic needle placement.

An example of a minimally invasive procedure that benefits from accurate needle placement is prostate brachytherapy. Prostate cancer is the second most common cancer among men in the U.S. [3] with an estimated 288,300 new cases and 34,700 deaths in 2023 [4]. High-Dose-Rate (HDR) brachytherapy is an internal and temporary radiotherapy method to remove cancerous tumors. Conventional HDR brachytherapy involves placement of radiation sources close to the tumor using rigid, straight needles. Although the conventional method has been promising [5]–[9] in terms of tumor control, toxicities, overall costs, and effectiveness (e.g., 5-yr and 10-yr distant metastasis-free survival rates) [10]–[14], studies have reported side-effects such as edema in tissue, incontinence, and impotence. The side effects are a result of excessive radiation and needle penetration into sensitive organs such as the urethra, bladder, rectum, penile bulb, cavernous veins, and neuro-vascular bundles. Also, use of HDR brachytherapy is limited in patients whose pubic arch obstructs the transperineal path to the prostate, thereby interfering with needle placement [15]. A study showed that the procedure was practical only for 24 out of the 40 patients studied due to pelvic bone arch interference [16]. Even a narrow pubic arch may prevent proper implantation in a small prostate gland [17]. Known strategies to overcome this problem such as oblique catheter insertion and pelvic rotation [18], [19] are not optimal. Active tendon-driven needles [20] have shown promises to alleviate this concern via their precise navigation in desired trajectories.

On another note, imprecise catheter implantation often causes insufficient dosage to the cancer and/or inadvertent radiation of the rectum, urethra, and bladder. The former causes failure of treatment, while the latter results in adverse side effects like rectal ulceration, incontinence, and dysuria (painful urination). Increased doses to normal structures is well correlated with increased toxicity after brachytherapy, and despite the adoption of modern techniques, toxicity remains significant [21].

Figures 1a & 1b show an US image of an anonymized patient's prostate gland, where the boundaries of the prostate are marked by a urologist. In conventional prostate brachytherapy, needles are inserted in straight trajectories (examples are shown in Figure 1a with dashed lines) using conventional straight and rigid needles; however, conformal to the patient's specific anatomy (shown in the figure with small triangles) are curved trajectories that are feasible to achieve using active flexible needles. Noting that most of the cancers are located at the peripheral zone of the prostate, placing radiation source(s) in nearby areas (marked in Figure 1b via the curved access channels of the active needles) is of great interest. In addition, active flexible needles provide the opportunity to move away from organs at risk (OARs) such as urethra, bladder, and rectum and thereby lower the risk of excess toxication. Figure 1b shows the prostate of the same patient when deformed due to a needle insertion. The small triangles in both figures are used to estimate the range of bending angle that an active needle should realize in a needle insertion task (explained in Section 2.1).

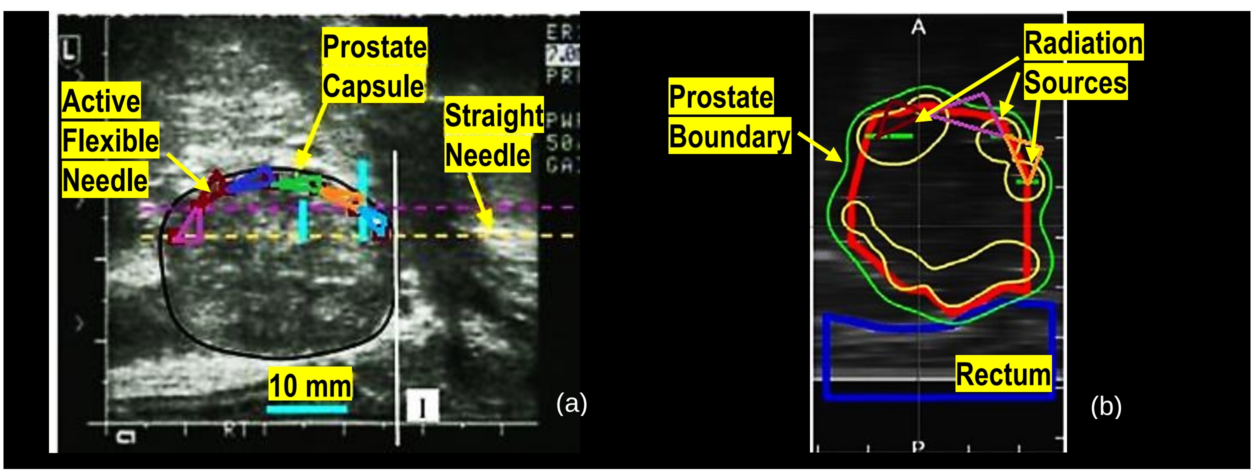

Figure 1. Straight vs. curved trajectories for needle insertion inside (a) undeformed, and (b) deformed prostate.

1.2. Background and related work

Researchers have been making efforts to introduce robotic needle insertion systems. For instance, Gerboni's group introduced a needle with high articulation by creating an asymmetric tendon-actuated flexible section in one direction [22], while Chitalia's group has improved on the design by combining different notch patterns on a single needle [23]. The group later proposes two distinct flexible sections along with a tendon-routing block to minimize errors involving a misalignment issue [24]. Concerning efforts related to imaging modalities, Kriger, et al. developed an MRI-compatible system with a hybrid tracking method that eliminated the need for performing manipulator motions inside the scanner while still retaining accuracy [25] and Khadem's group proposed a method to estimate a passive needle tip's trajectory using 2D transverse US images [26].

Besides needle actuation, intraoperative tracking of the needle and tissue is of great importance. Robotic closed-loop control of the needles navigating inside tissue relies on the feedback of the needle tip position and/or the needle shape. Since the needles should ultimately perform percutaneous procedures in nontransparent human tissue, vision-based (camera) tracking is unrealistic. On the other hand, use of position/shape sensors is not desired due to the small (meso-scale) size of the needle. Thus, US or MRI imaging feedback are ideal candidates for needle tip and shape tracking; however, intraoperative image acquisition and processing to have reliable feedback in real-time is challenging.

Recent research efforts have introduced needle-tissue interaction models to predict the needle behavior inside tissue. For example, a mechanics-based dynamic model was introduced [27] to estimate deflection of a bevel-tip flexible needle while inserted into soft tissues. In a later study, an overview of this dynamic model was presented with comments about controllability of flexible needle insertions [28]. In another work [29], a needle insertion model with mechanics of tissue rupture, and effect of insertion velocity on needle force, tissue deformation, and needle work was presented. Another study in 2012 [30], introduced a mechanics-based model for needle deflection with multiple bends during insertion into soft tissue based on a Rayleigh-Ritz formulation. A later study in 2015 [31] the beam theory was extended to develop a new mechanics-based dynamic model for needle insertion in soft tissue. More recent works [32], [33] presented an estimator to predict needle tip deflection and needle shape during needle insertion into soft tissue. Finite element methods have also been developed to model needle-tissue interactions using a discretized model of the needle and tissue [34], [35]. A nonholonomic model for steering flexible needles with bevel tips was developed in [36] for needle control with actuations at the base of the needle. Another study in 2015 [37] presented an extension to the kinematic bicycle model for bevel-tipped needle motion in soft tissue, accounting for non-constant curvature paths for the needle tip. The models are intended to be used in model-based control of the needle while navigating inside tissue towards a moving target. However, models are associated with errors, and could not be trusted without additional sensory feedback and a proper controller. This work presents real-time and reliable estimation of the needle tip to realize a closed-loop control of the needle movement inside tissue.

Dexterity and visualization of robotic instruments are key factors in the procedure's success. Recent research has been focused on improving *flexibility* of the instruments as well as *sensing and visualization* of the instruments inside the body. Examples of robotic tools with improved flexibility include tendon-driven notched needles [41], [42], steerable guidewires [43], continuum robotic tool [23], [44], concentric tubes [45], [46], and 3D printed active flexible needles [47], [48]. To the best of our knowledge, none of the above-mentioned active needles are specifically designed and developed for prostate brachytherapy.

Several sensing and visualization techniques have also been developed to provide feedback to the operating surgeon of the robotic systems. Recent progress in sensing and visualization of the robotic tools include US tip tracking [49]–[51], shape prediction [52]–[54], Fiber Bragg Gratings (FBG) based force estimation and shape sensing [55], [56] and shape memory alloy (SMA) self-shape and self-force sensing [57], [58]. Our group has previously published works on needle actuation. In one work, we studied the performance and interactive response of multiple distributed SMA actuators to manipulate a 3D printed active flexible needle [59]. In another work, Karimi and Konh developed an electrical resistance feedback control of multiple SMA actuators to control the movement of a 3D steerable active needle [60] in a tissue phantom.

This work presents two tendon-driven active needles to achieve a robotic bidirectional bending inside the tissue. The active needle consists of a flexure section, carefully designed, for improved flexibility inside the prostate gland. The needle's bidirectional bending is realized via independent actuation of two internal tendons. A closed-loop control framework is provided to use real-time US tracking in water medium and electromagnetic (EM) tracking in air as position feedback of the tool's tip for closed-loop control. Ultimately, the performance of the active needle in a water medium is evaluated to assess if the US tracking system can provide reliable position feedback to the controller for precise needle manipulation.

This manuscript is organized as follows: Section 1 provides an introduction about the needle insertion tasks and their challenges (Section 1.1), along with the background and related works in this area (Section 1.2). Section 2 lays out our robotic and control methods to improve the needle insertion tasks. Section 2.1 introduces our tendon-driven active needle, while Section 2.2 and 2.3 cover the actuation system to manipulate the active needle with US and EM tracking systems, respectively. Section 2.4 explains our closed-loop control method for precise manipulation of the active needle. Section 3 summarizes the results of the tendon displacement control in Section 3.1, and the active needle response using the US and EM tracking systems in Sections 3.2 and 3.3, respectively. Discussions and conclusions are outlined in Sections 4 and 5, respectively.

2. Materials and Methods

2.1. Robotic tendon-driven active needle

The design of the tendon-driven active needle is shown in Figure 2a. The active needle was developed by carving a series of six small notches on each side of a superelastic nitinol tube (Johnson Matthey, London, UK). Schematic dimensions of each notch are shown in Figure 2b with the corresponding values listed in Table 1.

Two active needles were developed in this work using the following manufacturing methods (i) ultraviolet (UV) laser cutter machine (Confluent Medical, Scottsdale, AZ) on the nitinol tube with 1.49mm inner diameter (ID) and 2.00mm outer diameter (OD) shown in Figure 2c, henceforth called the *US Tool*, and (ii) typical machining methods in lab on the nitinol tube with an ID of 1.60mm and OD of 2.00mm shown in Figure 2d, henceforth called *EM Tool*.

The US tool was made with a width of 0.46mm and depth of 1.68mm with higher precision offering more flexibility however at a high manufacturing cost. The EM Tool was fabricated in the lab using a Dremel to create notches that are approximately 0.42mm wide and 1.33mm deep at low manufacturing cost.

The notches produce a flexure section, shown in Figure 2a, that allows for improved flexibility of the active needle. Two holes (0.25mm in diameter) were made near the distal end of the flexure section for two tendons (0.10mm diameter SMA wires) to get attached to. The tendons were looped in and out of the holes and completely fixed to drive needle bending when pulled.

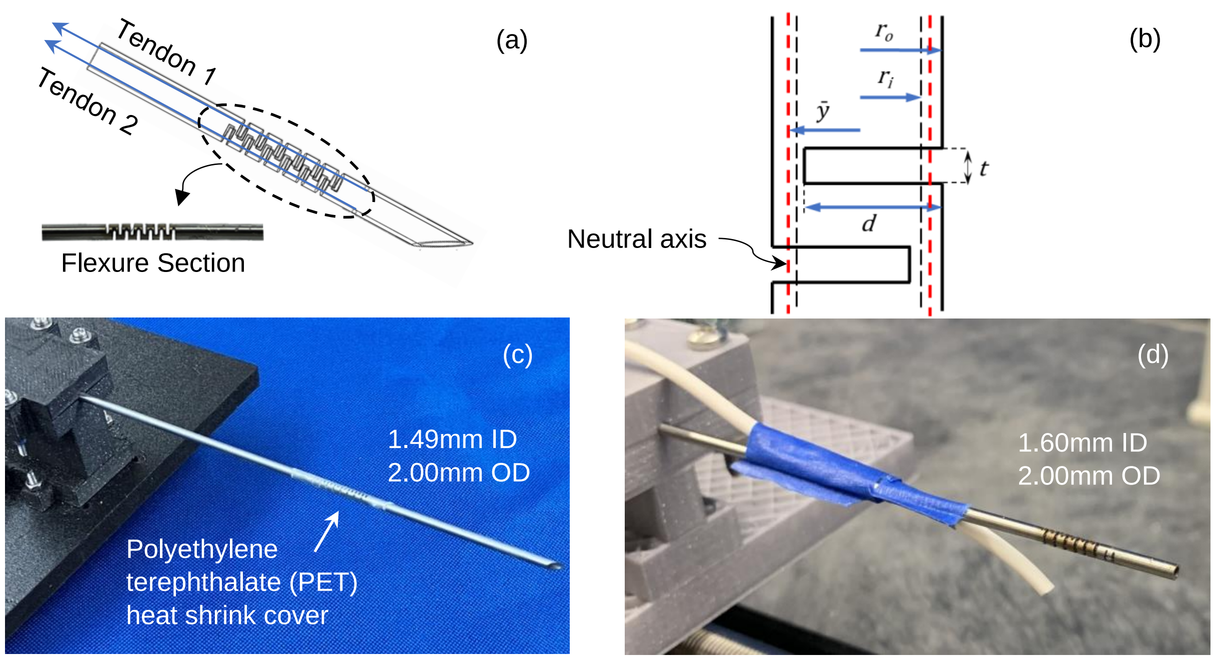

Figure 2. Schematic design of (a) tendon-driven active needle with (b) the notch dimensions fabricated on a nitinol tube using (c) UV laser cutter (US Tool), and (d) typical machining in our lab (EM Tool).

The flexure section of the needle was sealed to prevent tissue penetration into the needle tube and avoid tissue rupture. Shown in Figure 2c, the flexure section was covered (tight fit) with a Polyethylene terephthalate (PET) heat shrink tube (13μm thickness). The PET material is biocompatible and sterilizable with Ethylene oxide. We have tested the heat shrink tube on the active needle when bent and inserted into phantom tissues to ensure that it does not rip off during an insertion task [65]. The active needle including the covered flexure section is sterilizable.

The utmost expected angular deflection of the active needle to realize a curved trajectory inside prostate gland was estimated using Figure 1b, where a small radius of curvature is desired inside a deformed prostate. The bending angles were marked in the figure with small triangles on the curved trajectory, and the largest overall angular deflection of 50 degrees was measured. Methods to estimate the bending angles of the two active needles, developed in this work, are explained below.

The following equations are used to estimate the bending angle of the flexure section. For the notches schematically shown in Figure 2b, the neutral bending axis can be calculated using the following equation [66]:

$$\bar{y} = \frac{4({r_o}^3\, sin^3(\,\phi_o) - {r_i}^3\, sin^3(\,\phi_i))}{3\left({r_o}^2(2\phi_o - sin\,2\,\phi_o) - {r_i}^2(2\phi_i - sin\,2\,\phi_i)\right)} \quad (1)$$

where $\bar{y}$ is the distance moved from the center of the tube, r_o and r_i are the outer and inner radii of the tube, respectively, and ϕ_o and ϕ_i are found by the following equations:

$$\phi_o = arccos(\frac{d - r_o}{r_o}) \quad (2)$$

$$\phi_i = arccos(\frac{d - r_o}{r_i}) \quad (3)$$

where *d* is the notch depth. The bending angle for each notch can be estimated as:

$$\theta_i = \frac{h}{r_o + \bar{y}} \quad (4)$$

where *h* is the height of the neutral axis for each, which in this work is equal to the height of the cut (*t*). Assuming that the total deflection is distributed equally among the six notches, the bending angle of the whole flexible section could be found by multiplying the bending angle of each notch by the number of notches.

Table 1. The dimensions of the notches for the two active needles developed in this work. Units are in mm.

	$r_i\ (ID)$	$r_o\ (OD)$	d	t
US Tool	0.75 (1.49)	1.00 (2.00)	1.68	0.46
EM Tool	0.80 (1.60)	1.00 (2.00)	1.33	0.42

Dimensions of each notch for the two active needles are listed in Table 1. Using the equations above, the angular deflection of each notch for the US Tool and the EM Tool

14.48 and 14.13 degrees, respectively. The overall angular deflection of the flexure sections (six notches) 86.88 and 84.78 degrees for the US and EM Tools, respectively, which both surpass the expected angular deflection of 50 degrees for the active needle.

2.2. Actuation and ultrasound tracking system

The actuation system designed in this work consists of a motor, gear box, and lead screw. The tendon pulling force (*F*) to realize a specific bending on the flexure section when bending inside tissue should be estimated experimentally. The following equation is used to calculate the amount of torque (*T*) required to pull the tendon and consequently bend the active needle, similar to lowering down a load on a lead screw:

$$T = \frac{Fd_m}{2}\left(\frac{l + \pi f d_m \sec\alpha}{\pi d_m - fl \sec\alpha}\right) \quad (5)$$

where d_m, l, f, *and* α are the mean diameter of a single thread, tendon displacement, coefficient of friction, and thread angle, respectively. To provide an example of calculations for the active needle (shown in Figure 1b), we estimated that a maximum of 22N of force (tendon pulling force) is sufficient to bend the needle inside the tissue. This was estimated through needle insertion experiments in tissue phantoms with different Young's modulus [39] resembling prostate tissue. With this tension, an 8 mm diameter lead screw, friction coefficient of 0.25 for threaded pairs of a steel and dry screw, and thread angle of zero for square threads, the maximum torque was estimated as 0.41 N.m. Upon torque estimation, a DC motor, gear, and a lead screw combination was selected and purchased to develop a pulling actuation mechanism. To realize bi-directional bending on the active needle, two similar tendon actuation mechanisms were developed and installed to have full control over needle bending.

The experimental setup to actuate the active needle at a desired bending angle and real-time US tracking in water medium is shown in Figure 3a. The position of the tip is tracked using the US machine, processed through a series of image processing commands, and provided to the controller for appropriate control actions (explained later).

The actuation system to pull the internal tendons on the US Tool to realize a desired bidirectional bending at the tip (shown in Figure 3b) consists of two motors, each consisting of a 0.5W (Maxon Group, Sachseln, Switzerland) DC motor RE 8 Ø8 mm, Precious Metal Brushes with an 8mm diameter lead screw drive (GP 8 S Ø8mm, Metric spindle, M3 x 0.5), and an encoder (MR, Type S, 100CPT).

An L7 Linear Array US probe (CHISON Medical Technologies Co., Ltd., Jiangsu, China) was used to track the tip of the active needle in real time in water medium. The active needle was submerged in water with the US lying on the surface of the medium. For proper sealing, the inner walls of the 3D printed box (made by Prusa i3 MK3 printer), shown in Figure 3c, were coated with a silicone sealant (Gorilla Glue Co., Cincinnati, OH). To prevent water from entering the needle tube, wood putty (Minwax, Cleveland, OH) was used at the distal end surrounding the entry point of the needle.

Figure 3d shows the 2D plane of the US for tip tracking. The cross section of the needle appears as a circular shape in the US images. The US images are obtained in real time with a frame grabber, Epiphan Av.io HD. (Epiphan Systems, Ottawa, Canada) from the ECO 5 (CHISON Medical Technologies Co., Ltd., Jiangsu, China) through the US probe.

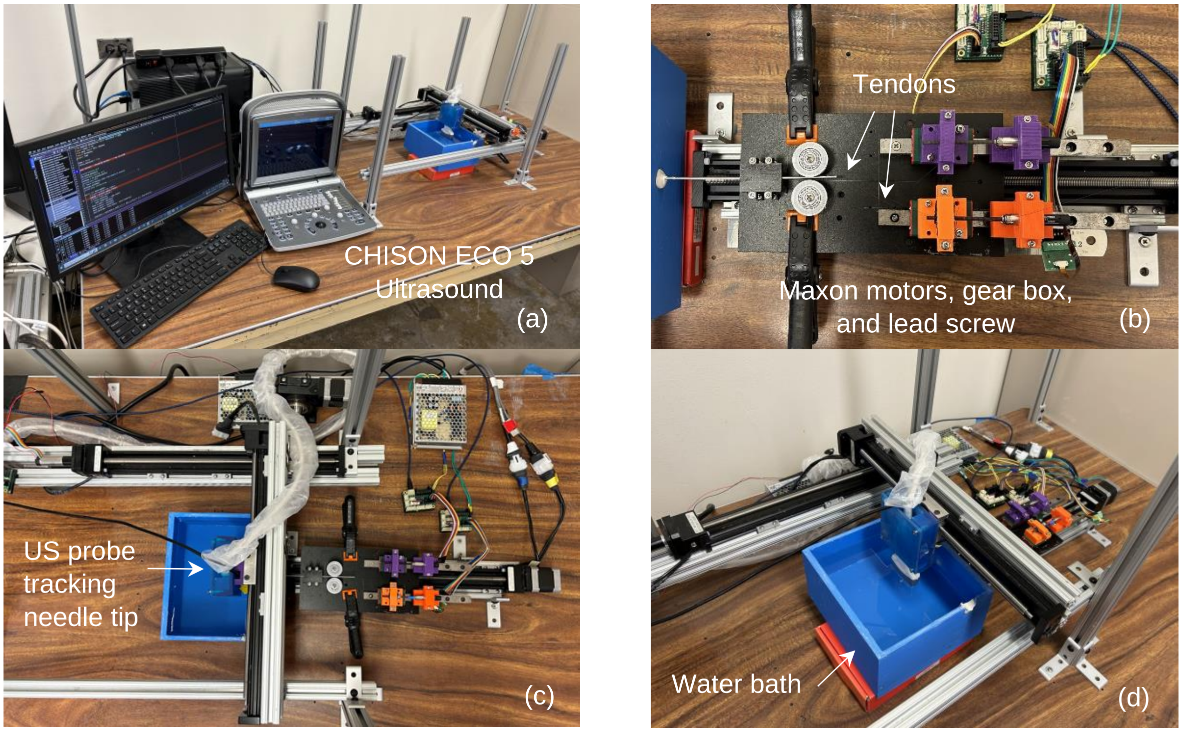

Figure 3. Experimental setup to evaluate performance of the tendon-driven active needle in water medium consisting of (a) US tracking, (b) tendon actuation system to bend the flexure section in two directions, (c) active needle and US submerged in water bath, and (d) 2D US plane for tracking bidirectional movement of the active needle tip.

Due to the artifacts observed in the US images while tracking the needle movement in the water medium, a series of image processing techniques (Figure 4a) were performed to obtain the 3D coordinates of the robotic tool in real time. Figure 4b shows an unprocessed US image, while Figure 4c shows the processed image where region of interest (ROI) is designated by the white box with the needle tip being marked with a red circle. The script assigned a coordinate system for the y-z plane over the US image being generated, using the pixel count as a basis for converting to millimeter scaling.

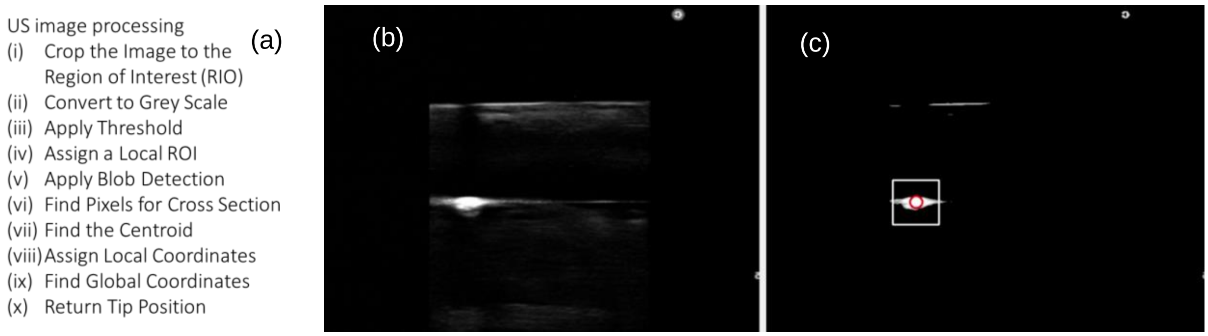

Figure 4. (a) Image processing method showing (b) unprocessed US images with sources of noise, and (c) processed US images in real time. The tip is marked with a red circle.

2.3. Actuation and electromagnetic tracking system

Another method of tracking the needle tip position was developed in this work using two 3D Guidance Model 55 EM tracking sensors (Northern Digital Inc., Waterloo, Canada), shown in Figure 5. The EM tracking system includes two sensors. The first and second sensors were installed inside the needle tube at the tip and the proximal end of the EM Tool, respectively. The EM tracker reports displacement and rotation data, so the bending angle at the flexure section of the active needle is measured directly through measuring the rotation of the distal sensor compared to the stationary proximal sensor. A similar actuation system, using Maxon motors as explained above, was used to manipulate the active needle. Manipulation and control were performed in the air.

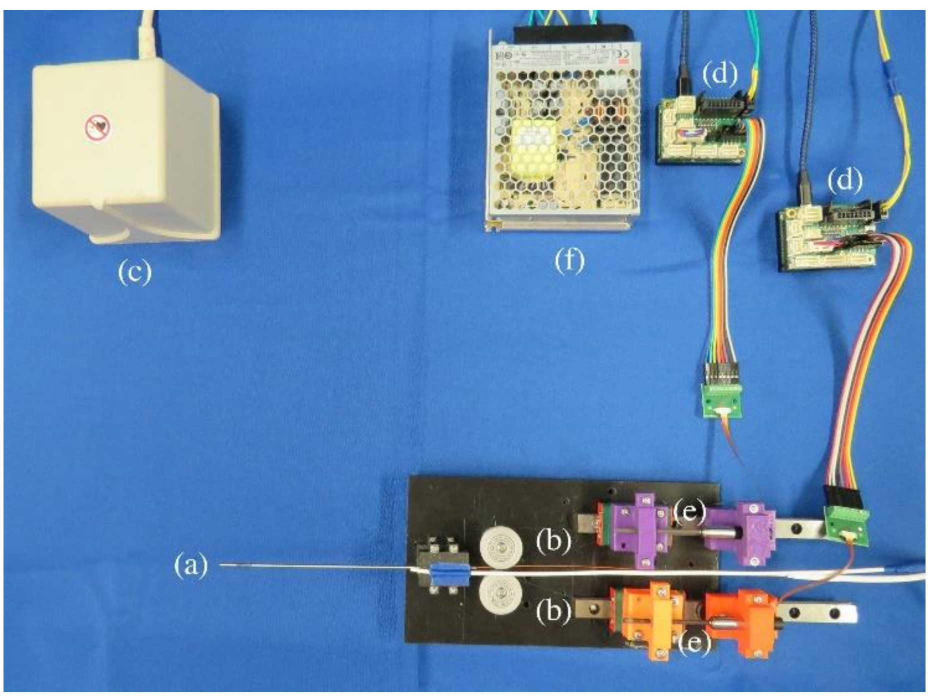

Figure 5. Actuation and EM tracking system consists of (a) active needle, (b) EM sensors, (c) EM transmitter, (d) EPOS4 positioning control boards, (e) two Maxon motors, and (f) power supply.

2.4. Closed-loop control

This section presents our controller to manipulate the tip of the active needle to follow a desired trajectory and reach a target point in water medium and air. Figure 6 shows a block diagram of our closed-loop control algorithm for US-based or EM-based method to realize a desired bending angle at the active needle's flexure section. The controller communicates with the actuation system to realize appropriate tendon displacements via actuation of the Maxon motors, and consequently realizes an angular deflection at the flexure section of the active needle. The controller was programmed to force the flexure section to follow an input desired bending angle function. The needle tip position obtained by the US tracking system, or the tip and distal positions of flexure section obtained by the EM tracking system were recorded in real time and used to estimate the angular bending of the flexure section. The PID controller compares the input desired function with the bending angle estimated obtained in real time from the US or the EM tracking system to adopt appropriate control actions.

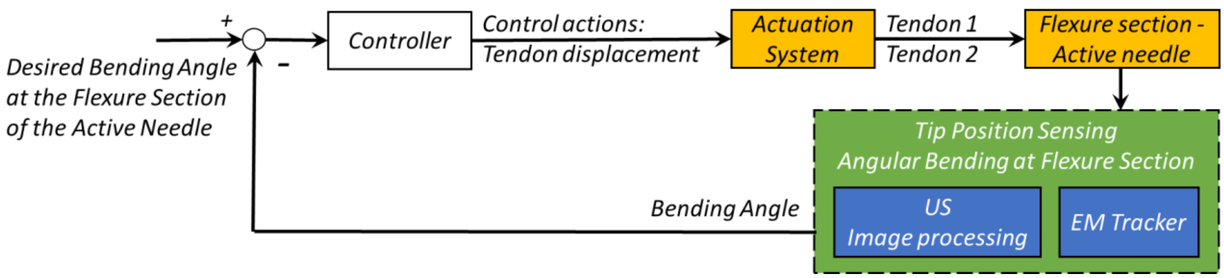

Figure 6. Scheme of closed-loop control method for realizing a desired bending angle at the flexure section of the robotic tool.

3. Results

3.1. Relationship between the tendon displacement and angular deflection

To characterize the flexure section, the tendons were linearly and independently displaced at increments of 0.5mm. Images were taken of the flexure section at each increment and the angular deflection was measured using ImageJ. Figure 7 shows the relationship between the linear displacement of the tendon with the angular deflection (bending) of the flexure section towards opposite directions (left and right). A second order polynomial function was fitted to the data, shown in Figure 7, to model the relationship between the tendon displacement and the angular deflection of the flexure section. This relationship was used by the controller to make decisions on the tendon displacement actions.

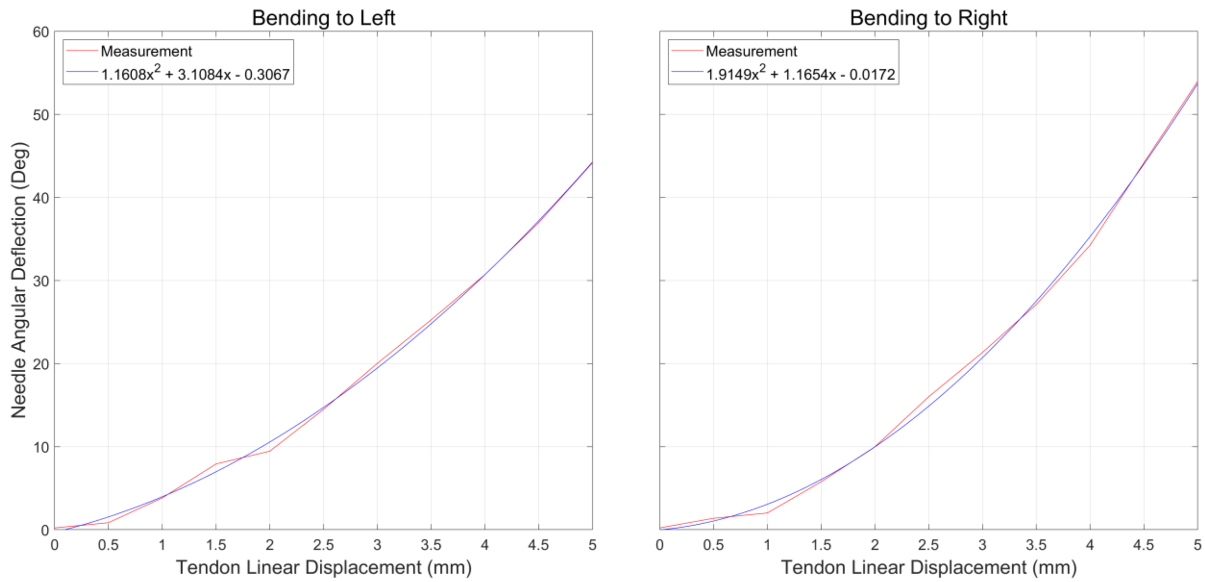

Figure 7. Relationship between angular deflection of the flexure section and the tendons' linear displacement.

3.2. Closed-loop control with US tracking feedback

To evaluate the performance of the active needle as well as the capability of our US tracking system to provide reliable feedback, the controller was set to realize a maximum angular bending of 10 degrees in a water medium. The coordinates of the needle tip were displayed on a computer running the US tracking script and recorded for graphical analysis post-experimentation. The coordinates were used to calculate the bending angle of the flexure section in real time. Time was also recorded during the experiment. The measured bending angle (output), as well as the desired bending angle (input) determined by the displacement function, were also recorded, analyzed, and compared. Three different input bending angle functions of (i) step, (ii) sine, and (iii) triangle were utilized for the flexure section to follow. The actual (green) and desired (red) bending angle of the flexure section was compared (Figure 8a) and the corresponding absolute difference (bending angle error) between the measured output and desired input was estimated and plotted (Figure 8b).

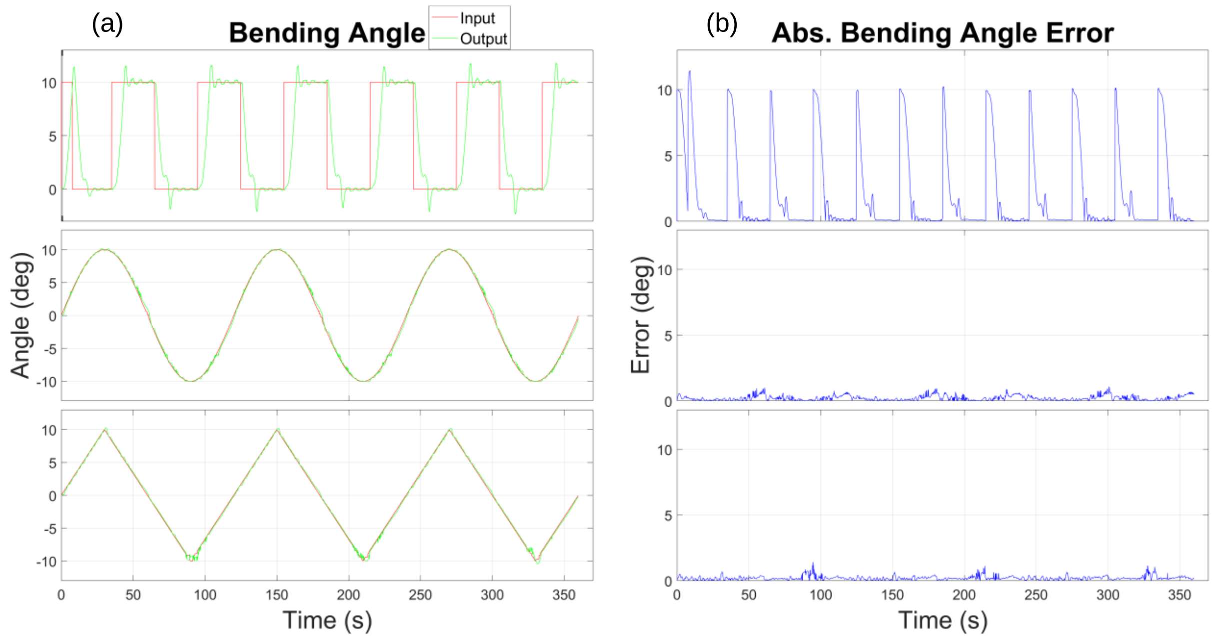

Figure 8. Bending angle of the tendon-driven active needle: (a) calculated from the data collected by the US tracking system for the different input functions, and (b) corresponding absolute difference (bending angle error) with respect to time.

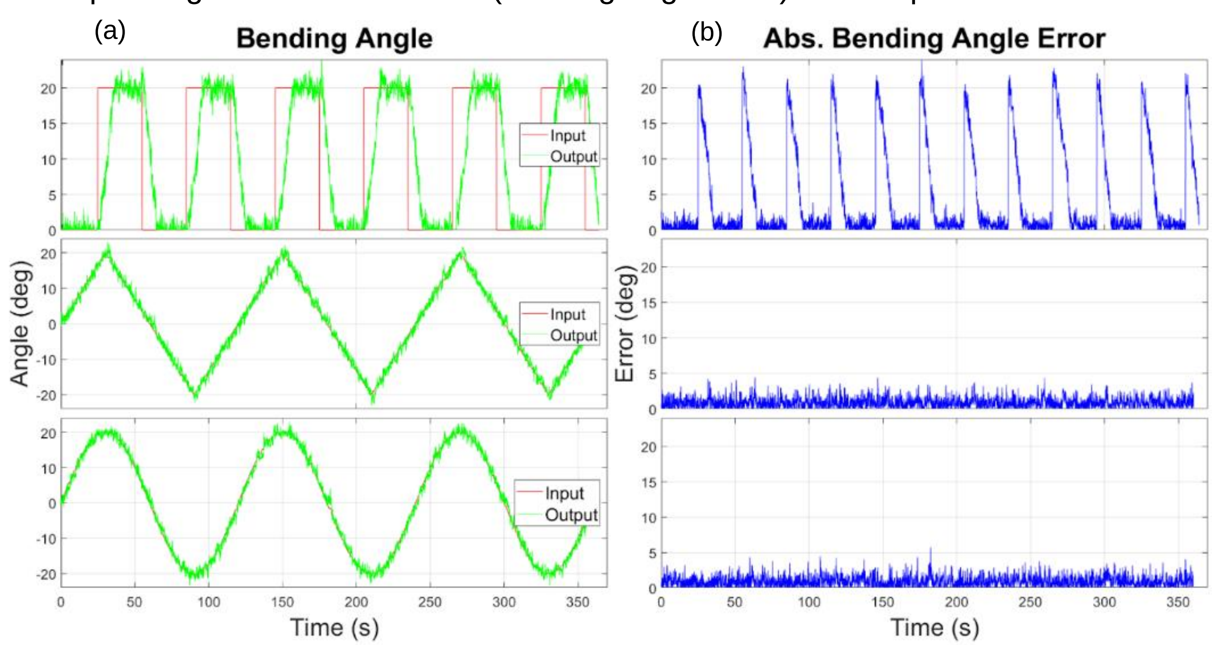

Figure 9. Bending angle of the tendon-driven active needle: (a) calculated from the data collected by the EM tracking system for the different input functions, and (b) corresponding absolute difference (bending angle error) with respect to time.

3.3. Closed-loop control with EM tracking feedback

To test the capability of the EM tracking system, the same displacement functions of (i) step, (ii) sine, and (iii) triangle were utilized for the needle tip to follow in the air. For comparison, the displacement function period was kept the same; however, since the EM tracker was capable of measuring higher deflection angles, the maximum deflection angle was set to 20 degrees. It was assumed that the difference in maximum angle would not greatly inhibit the function of the controller since the period was sufficiently long. The same method was used for data collection, analysis, and comparison. Figure 9a shows the controlled response of the flexure section with respect to the input functions, while Figure 9b shows the corresponding absolute difference (bending angle error) between the measured output and desired input.

4. Discussions

The EM tracking system produced similar position data to the US tracking; however, there was significantly more noise in the data. The angular deflection measurements with the EM tracker fluctuated routinely around ±2.0 degrees for very close data points, whereas the US tracking measurements hardly fluctuated (±0.5 degrees).

Table 2. Bending angle tracking error in closed-loop control of the active needle using the feedback received from US and EM Tracking systems. Units are in degrees.

Input Function	Tracking Method	Min. Error	Max. Error	Mean Error
Sine	US	1e-04	1.09	0.23
	EM	6e-04	4.54	1.00
Triangle	US	1e-04	1.42	0.21
	EM	8e-04	3.97	0.96
Step (ignoring delay)	US	4e-04	11.45 (2.33)	2.00 (0.27)
	EM	10e-04	22.91 (4.02)	4.51 (0.83)

Table 2 lists the maximum, minimum, and mean error for each input displacement function (i.e., sine, triangle, and step) using US and EM tracking systems. The controller was able to realize a sine displacement function with mean error values of 0.23 and 1.00 degrees with US and EM tracking systems, respectively. Tracking the triangular displacement function was done with 0.21 and 0.96 degrees of mean error values for the US and EM tracking systems, respectively. It was however noticed that the actuation system was incapable of producing a quick response for the step displacement function, and thereby a delayed response. Due to the relatively slow ramp-up time, mean error values were 2.00 and 4.51 degrees for the US and EM tracking systems, respectively. The highest maximum absolute error was observed to be 22.91 degrees from the EM tracking system following step function with the lowest coming from the sine function with the US system (1.09 degrees). As a consequence of the high absolute error, the largest mean error was also observed in the EM tracking step function with 4.51 degrees, and the lowest mean error was 0.21 degrees from the US tracking triangle function. The values in parentheses were estimated for the step function, when ignoring the delay period where the motors are running significantly behind the step. Once the measured angle was within the 10% of the desired step angle for the first time, data recording was resumed. The average delay period using the aforementioned parameters was 8.43 and 9.69 seconds for the US tracking and EM tracking systems, respectively. Ignoring the delay period, tracking of the step function resulted in mean error values of 0.27 and 0.83 degrees for the US and EM tracking systems, respectively, which closely align to the accuracies produced from the other displacement functions.

The mean error difference in tracking the desired bending angle of the active using the US or EM tracking systems were 0.77, 0.75, and 0.56 degrees for the sine, triangle, and step functions, respectively. The US tracking system realized a more accurate tracking of the active needle (average of 0.69 degrees improvement in accuracy) compared to the EM tracking for the three input functions used in this work. The results show that the US tracking system, submerged in the water, provides reliable feedback to the controller to realize a desired angular bending at the flexure section of the active needle with reasonable accuracy.

5. Conclusions

This work presents a closed-loop control of a bidirectional tendon-driven active needle in water medium and air using US and EM tracking, respectively. It has been observed that the bending angle of the active needle, could be controlled using position feedback of the US or the EM tracking system with corresponding absolute difference (bending angle error) <±1 degrees, and thereby comparable precisions. Therefore, the controller has been able to realize a desired bending angle at the flexure section of the active needle with reasonable accuracy using the US tracking system.

The US tracking system developed in this work is similar to the tracking method typically used in needle-based prostate interventions. It was shown that the controller is able to realize a desired bending angle at the flexure section of the active needle using the feedback of the US tracking system submerged in the water bath. This work takes the first step towards utilization of active tendon-driven needles in prostate interventions, where both the needle and the US are placed and function inside tissue.

Future work will focus on developing a closed-loop control to steer the active tendon-driven needle in a curved trajectory inside the prostate gland. Axial insertion of the needle to reach targets deep inside the tissue is also among our future aims. Introducing linear stages to the system will provide robotic movement to the US probe and provide more accuracy in tracking the needle tip in the event of larger tip displacements, which is often seen in patients with large prostate glands.

6. Competing interests

None declared.

7. Funding

Research reported in this publication was supported by the National Institute Of Biomedical Imaging And Bioengineering of the National Institutes of Health under Award

Number K25EB030562. The content is solely the responsibility of the authors and does not necessarily represent the official views of the National Institutes of Health.

8. Ethical approval

Not required.

9. References

[1] N. N. Stone, J. Roy, S. Hong, Y. C. Lo, and R. G. Stock, “Prostate gland motion and deformation caused by needle placement during brachytherapy,” *Brachytherapy*, vol. 1, no. 3, pp. 154–160, 2002, doi: 10.1016/S1538-4721(02)00058-2.

[2] S. Keereweer *et al.*, “Optical Image-guided Surgery—Where Do We Stand?,” *Mol. Imaging Biol.*, vol. 13, pp. 199–207, 2011, doi: 10.1007/s11307-010-0373-2.

[3] “USCS Data Visualizations - CDC.” https://gis.cdc.gov/Cancer/USCS/#/AtAGlance/.

[4] “American Cancer Society (ACS), cancer statistics center,” 2023. https://cancerstatisticscenter.cancer.org/?_ga=1.176033250.196666305.1484171292#!/.

[5] M. Fatyga *et al.*, “A comparison of HDR brachytherapy and IMRT techniques for dose escalation in prostate cancer: A radiobiological modeling study,” *Med. Phys.*, vol. 36, no. 9, pp. 3995–4006, 2009, doi: 10.1118/1.3187224.

[6] J. Hermesse *et al.*, “A dosimetric selectivity intercomparison of HDR brachytherapy, IMRT and helical tomotherapy in prostate cancer radiotherapy,” *Strahlentherapie und Onkol.*, vol. 185, no. 11, pp. 736–742, 2009, doi: 10.1007/s00066-009-2009-5.

[7] A. Challapalli, E. Jones, C. Harvey, G. O. Hellawell, and S. A. Mangar, “High dose rate prostate brachytherapy: An overview of the rationale, experience and emerging applications in the treatment of prostate cancer,” *Br. J. Radiol.*, vol. 85, no. SPEC. ISSUE 1, 2012, doi: 10.1259/bjr/15403217.

[8] J. Skowronek, “Brachytherapy in the therapy of prostate cancer - An interesting choice,” *Wspolczesna Onkol.*, vol. 17, no. 5, pp. 407–412, 2013, doi: 10.5114/wo.2013.38557.

[9] M. R. Cooperberg, D. P. Lubeck, M. V. Meng, S. S. Mehta, and P. R. Carroll, “The changing face of low-risk prostate cancer: Trends in clinical presentation and primary management,” *J. Clin. Oncol.*, vol. 22, no. 11, pp. 2141–2149, 2004, doi: 10.1200/JCO.2004.10.062.

[10] N. G. Thaker, T. N. Ali, M. E. Porter, T. W. Feeley, R. S. Kaplan, and S. J. Frank, “Communicating Value in Health Care Using Radar Charts: A Case Study of Prostate Cancer,” *J. Oncol. Pract.*, vol. 12, no. 9, pp. 813–820, 2016, doi: 10.1200/JOP.2016.011320.

[11] J. P. Ciezki *et al.*, “A comparison between low-dose-rate brachytherapy with or without androgen deprivation, external beam radiation therapy with or without

androgen deprivation, and radical prostatectomy with or without adjuvant or salvage radiation therapy for high-risk pros," *Int. J. Radiat. Oncol. Biol. Phys.*, vol. 97, no. 5, pp. 962–975, 2016, doi: 10.1016/j.ijrobp.2016.12.014.

[12] A. U. Kishan *et al.*, "Clinical outcomes for patients with Gleason score 9–10 prostate adenocarcinoma treated with radiotherapy or radical prostatectomy: a multi-institutional comparative analysis," *Eur. Urol.*, vol. 71, no. 5, pp. 766–773, 2017, doi: 10.1016/j.eururo.2016.06.046.

[13] C. Shah *et al.*, "Brachytherapy provides comparable outcomes and improved cost-effectiveness in the treatment of low/intermediate prostate cancer," *Brachytherapy*, vol. 11, no. 6, pp. 441–445, 2012, doi: 10.1016/j.brachy.2012.04.002.

[14] A. A. Laviana *et al.*, "Utilizing time-driven activity-based costing to understand the short- and long-term costs of treating localized, low-risk prostate cancer," *Cancer*, vol. 122, no. 3, pp. 447–455, 2016, doi: 10.1002/cncr.29743.

[15] K. Wallner, W. Ellis, K. Russell, W. Cavanagh, and J. Blasko, "Use of TRUS to predict pubic arch interference of prostate brachytherapy," *Int. J. Radiat. Oncol. Biol. Phys.*, vol. 43, no. 3, pp. 583–585, 1999, doi: 10.1016/S0360-3016(98)00459-3.

[16] P. Nickers, B. Thissen, N. Jansen, and J. M. Deneufbourg, "192Ir or 125I prostate brachytherapy as a boost to external beam radiotherapy in locally advanced prostatic cancer: A dosimetric point of view," *Radiother. Oncol.*, vol. 78, no. 1, pp. 47–52, 2006, doi: 10.1016/j.radonc.2005.09.002.

[17] J. Bellon, K. Wallner, W. Ellis, K. Russell, W. Cavanagh, and J. Blasko, "Use of pelvic CT scanning to evaluate pubic arch interference of transperineal prostate brachytherapy," *Int. J. Radiat. Oncol. Biol. Phys.*, vol. 43, no. 3, pp. 579–581, 1999, doi: 10.1016/S0360-3016(98)00466-0.

[18] S. A. Tincher *et al.*, "Effects of pelvic rotation and needle angle on pubic arch interference during transperineal prostate implants," *Int. J. Radiat. Oncol. Biol. Phys.*, vol. 47, no. 2, pp. 361–363, 2000, doi: 10.1016/S0360-3016(00)00434-X.

[19] B. Ryu *et al.*, "Prostate brachytherapy with oblique needles to treat large glands and overcome pubic arch interference," *Int. J. Radiat. Oncol. Biol. Phys.*, vol. 83, no. 5, pp. 1463–1472, 2012, doi: 10.1016/j.ijrobp.2011.10.012.

[20] B. Konh, B. Padasdao, Z. Batsaikhan, and J. Lederer, "Steering a Tendon-Driven Needle in High-Dose-Rate Prostate Brachytherapy for Patients with Pubic Arch Interference," in *International Symposium on Medical Robotics (ISMR)*, 2021, pp. 1–7.

[21] M. J. Zelefsky *et al.*, "Postimplantation dosimetric analysis of permanent transperineal prostate implantation: improved dose distributions with an intraoperative computer-optimized conformal planning technique," *Int. J. Radiat. Oncol. Biol. Phys.*, vol. 48, no. 2, pp. 601–608, 2000.

[22] G. Gerboni, J. D. Greer, P. F. Laeseke, G. L. Hwang, and A. M. Okamura, "Highly Articulated Robotic Needle Achieves Distributed Ablation of Liver Tissue," *IEEE*

Robot. Autom. Lett., vol. 2, no. 3, pp. 1367–1374, 2017, doi: 10.1109/LRA.2017.2668467.

[23] Y. Chitalia, S. Jeong, N. Deaton, J. J. Chern, and J. P. Desai, “Design and Kinematics Analysis of a Robotic Pediatric Neuroendoscope Tool Body,” *IEEE/ASME Trans. Mechatronics*, vol. 25, no. 2, pp. 985–995, 2020, doi: 10.1109/TMECH.2020.2967748.

[24] Y. Chitalia, S. Jeong, K. K. Yamamoto, J. J. Chern, and J. P. Desai, “Modeling and Control of a 2-DoF Meso-Scale Continuum Robotic Tool for Pediatric Neurosurgery,” *IEEE Trans. Robot.*, vol. 37, no. 2, pp. 520–531, 2020, doi: 10.1109/tro.2020.3031270.

[25] A. Krieger *et al.*, “An MRI-compatible robotic system with hybrid tracking for MRI-guided prostate intervention,” *IEEE Trans. Biomed. Eng.*, vol. 58, no. 11, pp. 3049–3060, Nov. 2011, doi: 10.1109/TBME.2011.2134096.

[26] M. Khadem, C. Rossa, R. S. Sloboda, N. Usmani, and M. Tavakoli, “Ultrasound-Guided Model Predictive Control of Needle Steering in Biological Tissue,” *J. Med. Robot. Res.*, vol. 01, no. 01, p. 1640007, 2016, doi: 10.1142/s2424905x16400079.

[27] A. Haddadi and K. Hashtrudi-Zaad, “Development of a dynamic model for bevel-tip flexible needle insertion into soft tissues,” *Proc. Annu. Int. Conf. IEEE Eng. Med. Biol. Soc. EMBS*, pp. 7478–7482, 2011, doi: 10.1109/IEMBS.2011.6091845.

[28] A. Haddadi, O. Goksel, S. E. Salcudean, and K. Hashtrudi-Zaad, “On the controllability of dynamic model-based needle insertion in soft tissue,” *2010 Annu. Int. Conf. IEEE Eng. Med. Biol. Soc. EMBC’10*, pp. 2287–2291, 2010, doi: 10.1109/IEMBS.2010.5627676.

[29] M. Mahvash and P. E. Dupont, “Mechanics of dynamic needle insertion into a biological material,” *IEEE Trans. Biomed. Eng.*, vol. 57, no. 4, pp. 934–943, 2010, doi: 10.1109/TBME.2009.2036856.

[30] R. J. Roesthuis, M. Abayazid, and S. Misra, “Mechanics-based model for predicting in-plane needle deflection with multiple bends,” *2012 4th IEEE RAS EMBS Int. Conf. Biomed. Robot. Biomechatronics*, pp. 69–74, 2012, doi: 10.1109/BioRob.2012.6290829.

[31] M. Khadem, B. Fallahi, C. Rossa, R. S. Sloboda, N. Usmani, and M. Tavakoli, “A mechanics-based model for simulation and control of flexible needle insertion in soft tissue,” in *IEEE International Conference on Robotics and Automation*, 2015, pp. 2264–2269, doi: 10.1109/ICRA.2015.7139499.

[32] T. Lehmann, C. Rossa, N. Usmani, R. S. Sloboda, and M. Tavakoli, “A Real-Time Estimator for Needle Deflection During Insertion Into Soft Tissue Based on Adaptive Modeling of Needle-Tissue Interactions,” *IEEE/ASME Trans. Mechatronics*, vol. 21, no. 6, pp. 2601–2612, 2016, doi: 10.1109/TMECH.2016.2598701.

[33] C. Rossa, M. Khadem, R. Sloboda, N. Usmani, and M. Tavakoli, “Adaptive Quasi-Static Modelling of Needle Deflection during Steering in Soft Tissue,” *IEEE Robot.*

Autom. Lett., vol. 1, no. 2, pp. 916–923, 2016, doi: 10.1109/LRA.2016.2527065.

[34] O. Goksel, S. E. Salcudean, and S. P. Dimaio, “3D simulation of needle-tissue interaction with application to prostate brachytherapy,” *Comput. Aided Surg.*, vol. 11, no. 6, pp. 279–288, 2006, doi: 10.3109/10929080601089997.

[35] O. Goksel, E. Dehghan, and S. E. Salcudean, “Modeling and simulation of flexible needles,” *Med. Eng. Phys.*, vol. 31, no. 9, pp. 1069–1078, 2009, doi: 10.1016/j.medengphy.2009.07.007.

[36] R. J. Webster *et al.*, “Nonholonomic modeling of needle steering,” *Int. J. Rob. Res.*, vol. 25, no. 5–6, pp. 509–525, 2006, doi: 10.1177/0278364906065388.

[37] B. Fallahi, M. Khadem, C. Rossa, R. Sloboda, N. Usmani, and M. Tavakoli, “Extended bicycle model for needle steering in soft tissue,” in *IEEE International Conference on Intelligent Robots and Systems*, 2015, pp. 4375–4380, doi: 10.1109/IROS.2015.7353998.

[38] A. Leibinger *et al.*, “Soft Tissue Phantoms for Realistic Needle Insertion: A Comparative Study,” *Ann. Biomed. Eng.*, vol. 44, no. 8, pp. 2442–2452, 2016, doi: 10.1007/s10439-015-1523-0.

[39] N. V Datla *et al.*, “Polyacrylamide phantom for self-actuating needle-tissue interaction studies,” *Med. Eng. Phys.*, vol. 36, no. 1, pp. 140–145, 2014, doi: 10.1016/j.medengphy.2013.07.004.

[40] B. Ruiz, P. Hutapea, K. Darvish, A. Dicker, Y. Yu, and T. Podder, “WE-A-108-08: Development of Shape Memory Alloy Actuated Flexible Needle Control System for Prostate Brachytherapy,” *Med. Phys.*, vol. 40, no. 6Part28, p. 467, Jun. 2013, doi: https://doi.org/10.1118/1.4815501.

[41] M. Khadem, C. Rossa, N. Usmani, R. S. Sloboda, and M. Tavakoli, “Introducing notched flexible needles with increased deflection curvature in soft tissue,” *IEEE/ASME Int. Conf. Adv. Intell. Mechatronics, AIM*, vol. 2016-Septe, pp. 1186–1191, 2016, doi: 10.1109/AIM.2016.7576931.

[42] B. Padasdao, S. Lafreniere, M. Rabiei, Z. Batsaikhan, and B. Konh, “Teleoperated and Automated Control of a Robotic Tool for Targeted Prostate Biopsy,” *Jounral Med. Robot. Res.*, 2023, doi: 10.1142/S2424905X23400020.

[43] S. Jeong, Y. Chitalia, and J. P. Desai, “Design, Modeling, and Control of a Coaxially Aligned Steerable (COAST) Guidewire Robot,” *IEEE Robot. Autom. Lett.*, vol. 5, no. 3, pp. 4947–4954, 2020, doi: 10.1109/LRA.2020.3004782.

[44] J. Burgner-Kahrs, D. C. Rucker, and H. Choset, “Continuum Robots for Medical Applications: A Survey,” *IEEE Trans. Robot.*, vol. 31, no. 6, pp. 1261–1280, 2015, doi: 10.1109/TRO.2015.2489500.

[45] T. E. Ertop *et al.*, “Towards Suturing from Within the Urethra Using Concentric Tube Robots: First Experiences in Biological Tissues,” *2022 Int. Symp. Med. Robot. ISMR 2022*, 2022, doi: 10.1109/ISMR48347.2022.9807548.

[46] J. B. Gafford *et al.*, “A Concentric Tube Robot System for Rigid Bronchoscopy: A Feasibility Study on Central Airway Obstruction Removal,” *Ann. Biomed. Eng.*,

vol. 48, no. 1, pp. 181–191, 2020, doi: 10.1007/s10439-019-02325-x.

[47] Z. K. Varnamkhasti and B. Konh, “Design, Fabrication, and Testing of a Flexible Three-Dimensional Printed Percutaneous Needle with Embedded Actuators,” *ASME J. Med. Devices*, vol. 15, no. 2, p. 021007 (10 pages), 2020.

[48] Z. K. Varnamkhasti and B. Konh, “Compact 3D-Printed Active Flexible Needle for Percutaneous Procedures,” *Surg. Innov.*, vol. 27, no. 4, pp. 402–405, 2020, doi: 10.1177/1553350620945564.

[49] B. Padasdao, Z. K. Varnamkhasti, and B. Konh, “3D Steerable Biopsy Needle with a Motorized Manipulation System and Ultrasound Tracking to Navigate inside Tissue,” *J. Med. Robot. Res.*, vol. 5, no. 03n04, p. 2150003, 2020, doi: 10.1142/S2424905X21500033.

[50] M. Khadem, C. Rossa, N. Usmani, R. S. Sloboda, and M. Tavakoli, “Semi-Automated Needle Steering in Biological Tissue Using an Ultrasound-Based Deflection Predictor,” *Ann. Biomed. Eng.*, vol. 45, no. 4, pp. 924–938, 2017, doi: 10.1007/s10439-016-1736-x.

[51] G. J. Vrooijink, M. Abayazid, S. Patil, R. Alterovitz, and S. Misra, “Needle path planning and steering in a three-dimensional non-static environment using two-dimensional ultrasound images,” *Int. J. Rob. Res.*, vol. 33, no. 10, pp. 1361–1374, 2014, doi: 10.1177/0278364914526627.

[52] B. Konh, B. Padasdao, Z. Batsaikhan, and S. Y. Ko, “Integrating robot-assisted ultrasound tracking and 3D needle shape prediction for real-time tracking of the needle tip in needle steering procedures,” *Int. J. Med. Robot. Comput. Assist. Surg.*, vol. 17, no. 4, p. e2272, 2021, doi: 10.1002/rcs.2272.

[53] J. Carriere, C. Rossa, R. Sloboda, N. Usmani, and M. Tavakoli, “Real-time needle shape prediction in soft-tissue based on image segmentation and particle filtering,” *IEEE/ASME Int. Conf. Adv. Intell. Mechatronics, AIM*, vol. 2016-Septe, pp. 1204–1209, 2016, doi: 10.1109/AIM.2016.7576934.

[54] B. Konh, Z. Batsaikhan, and B. Padasdao, “3D shape estimation of an active needle inside tissue using 2D ultrasound images,” in *Design of Medical Devices Conference*, 2021, pp. 1–4.

[55] T. A. Brumfiel, A. Sarma, and J. P. Desai, “Towards FBG-based End-Effector Force Estimation for a Steerable Continuum Robot,” *Int. Symp. Med. Robot.*, 2022.

[56] Y. Chitalia, N. J. Deaton, S. Jeong, N. Rahman, and J. P. Desai, “Towards FBG-Based Shape Sensing for Micro-Scale and Meso-Scale Continuum Robots with Large Deflection,” *IEEE Robot. Autom. Lett.*, vol. 5, no. 2, pp. 1712–1719, 2020, doi: 10.1109/LRA.2020.2969934.

[57] S. Karimi and B. Konh, “Kinematics Modelling and Dynamics Analysis of an SMA-Actuated Active Flexible Needle for Feedback-Controlled Manipulation in Phantom,” *Med. Eng. Phys.*, vol. 107, p. 103846, 2022.

[58] S. Karimi and B. Konh, “Self-Sensing Feedback Control of Multiple Interacting

Shape Memory Alloy Actuators in a 3D Steerable Active Flexible Needle," *J. Intell. Mater. Syst. Struct.*, vol. 31, no. 12, pp. 1524–1540, 2020.

[59] B. Padasdao and B. Konh, "Shape Memory Alloy Actuators in an Active Needle - Modeling , Precise Assembly, and Performance Evaluation," *J. Manuf. Sci. Eng.*, vol. 143, no. 2, p. 021003 (10 pages), 2020.

[60] B. Konh, P. Berkelman, and S. Karimi, "Needle Tip Manipulation and Control of a 3D Steerable SMA-Activated Flexible Needle," 2020.

[61] B. Padasdao, Z. K. Varnamkhasti, and B. Konh, "3D Steerable Biopsy Needle with a Motorized Manipulation System and Ultrasound Tracking to Navigate inside Tissue," *J. Med. Robot. Res.*, vol. 05, no. 03n04, pp. 2150003-1-2150003–18, 2021, doi: 10.1142/S2424905X21500033.

[62] B. Padasdao, Z. Batsaikhan, S. Lafreniere, M. Rabiei, and B. Konh, "Modeling and Operator Control of a Robotic Tool for Bidirectional Manipulation in Targeted Prostate Biopsy," in *International Symposium on Medical Robotics (ISMR)*, 2022, pp. 1–7.

[63] B. Konh, B. Padasdao, Z. Batsaikhan, and S. Y. Ko, "Integrating robot-assisted ultrasound tracking and 3D needle shape prediction for real-time tracking of the needle tip in needle steering procedures," *Int. J. Med. Robot. Comput. Assist. Surg.*, vol. 17, no. 4, 2021, doi: 10.1002/rcs.2272.

[64] B. Padasdao, Z. Batsaikhan, D. Brown, and J. Moore, "Estimation of tissue movement in needle insertion tasks using an active needle," in *Design of Medical Devices Conference*, 2022, pp. 1–5.

[65] B. Padasdao, S. Lafreniere, M. Rabiei, Z. Batsaikhan, and B. Konh, "Teleoperated and Automated Control of a Robotic Tool for Targeted Prostate Biopsy," *J. Med. Robot. Res.*, 2022.

[66] K. W. Eastwood *et al.*, "Design of a contact-aided compliant notched-tube joint for surgical manipulation in confined workspaces," *J. Mech. Robot.*, vol. 10, no. 1, pp. 1–12, 2018, doi: 10.1115/1.4038254.